OPTICS

Polarization vortices of thermal emission

Ye Zhang[1]†, Qiang Wang[1]*†, Meng Xiao[2,3]*, Tao Liu[2], Fan Zhong[4], Zhenxin Lai[1], Shining Zhu[1], Hui Liu[1,5]*

Polarization vortices, crucial constituents of singular optics, manifest as vortices of polarization states around singularities. Recent progress has linked polarization vortices with bound states in the continuum (BICs) in optical waves. However, this association has not been explored in the realm of thermal emission, which holds the potential for generating arbitrary polarizations in a single thermal emitter. Here, we implement a polarization vortex thermal emitter (PVTE) based on BICs in a photonic crystal slab (PCS), allowing for the generation of various polarization states simultaneously along different directions. Using a custom-designed polarized angle-resolved thermal emission spectrometer (PARTES), we experimentally confirm polarization vortices of thermal emission originating from BICs with different charges and types. The proposed PVTEs present effective strategies for controlling thermal emission and show promising applications in infrared optical technology.

INTRODUCTION

In recent years, there has been notable strides in manipulating thermal emission through artificial metamaterials (*1*–*3*). Diverse thermal emitters (*4*, *5*), each having unique characteristics, have been developed for applications in radiative cooling (*6*–*9*), energy harvesting (*10*), infrared sensing (*11*), and thermal camouflage (*12*, *13*). The manipulation of thermal emission can target its spectrum (*14*–*16*), angular selectivity (*17*, *18*), dynamical control (*12*, *13*), near-field heat transfer (*19*, *20*), nonreciprocal effect (*21*–*23*), and polarization (*24*–*30*). Notably, controlling polarization in thermal emission offers distinct capabilities with broad applications. For instance, thermal emission from antennas and gratings can achieve nearly pure linear polarization (*24*, *27*, *28*) to enhance energy efficiency (*31*–*33*). Recent breakthroughs have demonstrated the generation of circularly polarized thermal emission with achiral or chiral metamaterials (*25*, *26*, *29*, *30*), leading to advancements in chiral-selective detection. Nolen *et al.* (*34*) experimentally demonstrated arbitrary single or dual polarized thermal emission by pointwise design of the thermal metasurface. However, in most reported studies to date, thermal emission control is primarily achieved through local resonance modes in real-space, with each structure capable of radiating only a limited number of polarized thermal emission modes. Expanding the range of polarized thermal emissions typically requires the design and fabrication of multiple distinct structures. At present, no methods exist for the continuous tuning of an infinite number of thermal emission modes within a single periodic structure, making it challenging to flexibly achieve arbitrary linear polarizations within a single emitter. In addition, polarization vortices (*35*, *36*), techniques for flexible polarization control, have been successfully applied in various fields since their discovery. However, they have not yet been explored in thermal emission, which could enable a single thermal emitter to provide versatile polarizations, thus facilitating the integration of fully polarization-controlled thermal emission.

In recent research endeavors, the fascination with bound states in the continuum (BICs) has surged, propelled by their extraordinary capability to manipulate optical waves (*37*–*41*). BICs are characterized as localized states that coexist with a continuous spectrum of extending waves (*42*–*45*). Researchers have explored their various applications (*46*), including lasing (*47*, *48*), enhancing nonlinear effects (*49*), and refining light-matter interactions (*50*). Notably, BICs in photonic crystal slabs (PCSs) often exhibit nontrivial topological charges accompanied by polarization vortices, which has been explored both theoretically (*51*) and experimentally (*52*). The unique attributes of these polarization vortices have widespread applications in governing the polarization of outgoing optical waves (*53*–*58*), such as vortex lasers (*59*, *60*) and vortex beams (*61*). Despite aforementioned substantial progress, the generation of vortex thermal emission through BICs remains an unexplored frontier.

In this work, we demonstrate a polarization vortex thermal emitter (PVTE) using BICs in a PCS. Unlike previous designs, which were limited to specific polarizations for one emitter, the PVTE herein can offer controllable diverse polarizations along different emission directions. More precisely, arbitrary linearly polarized emissions could be achieved from a single PVTE by encircling BICs in momentum space. We use a self-developed polarized angle-resolved thermal emission spectrometer (PARTES) system to calibrate the polarization vortex. In experimental observations, we identify polarization vortices of thermal emission originating from BICs, characterized by different topological charges that include both symmetry-protected and accidental BICs. The PVTE exhibits potential applications in various scenarios for on-chip integration, such as microinfrared sensing and microthermal imaging.

RESULTS

Design and simulation

To achieve the PVTE, we used a PCS with a square lattice and a period of $\Lambda = 5$ μm in Fig. 1A. A germanium (Ge) slab, with a thickness of $h_{Ge} = 1.6$ μm, is deposited on a gold (Au) layer with a thickness of $h_{Au} = 0.2$ μm. Subsequently, an array of cylindrical air holes, with a diameter of $D = 3$ μm and a height of h_{Ge} (equivalent

[1]National Laboratory of Solid State Microstructures, Jiangsu Physical Science Research Center, School of Physics, Collaborative Innovation Center of Advanced Microstructures, Nanjing University, Nanjing 210093, China. [2]School of Physics and Technology, and Key Laboratory of Artificial Micro- and Nano-structures of Ministry of Education, Wuhan University, Wuhan 430072, China. [3]Wuhan Institute of Quantum Technology, Wuhan 430206, China. [4]School of Physics, Key Laboratory of Quantum Materials and Devices of Ministry of Education, Southeast University, Nanjing 211189, China. [5]School of Science, Harbin University of Science and Technology, Harbin 150080, China.
*Corresponding author. Email: q.wang@nju.edu.cn (Q.W.); phmxiao@whu.edu.cn (M.X.); liuhui@nju.edu.cn (H.L.)
†These authors contributed equally to this work.

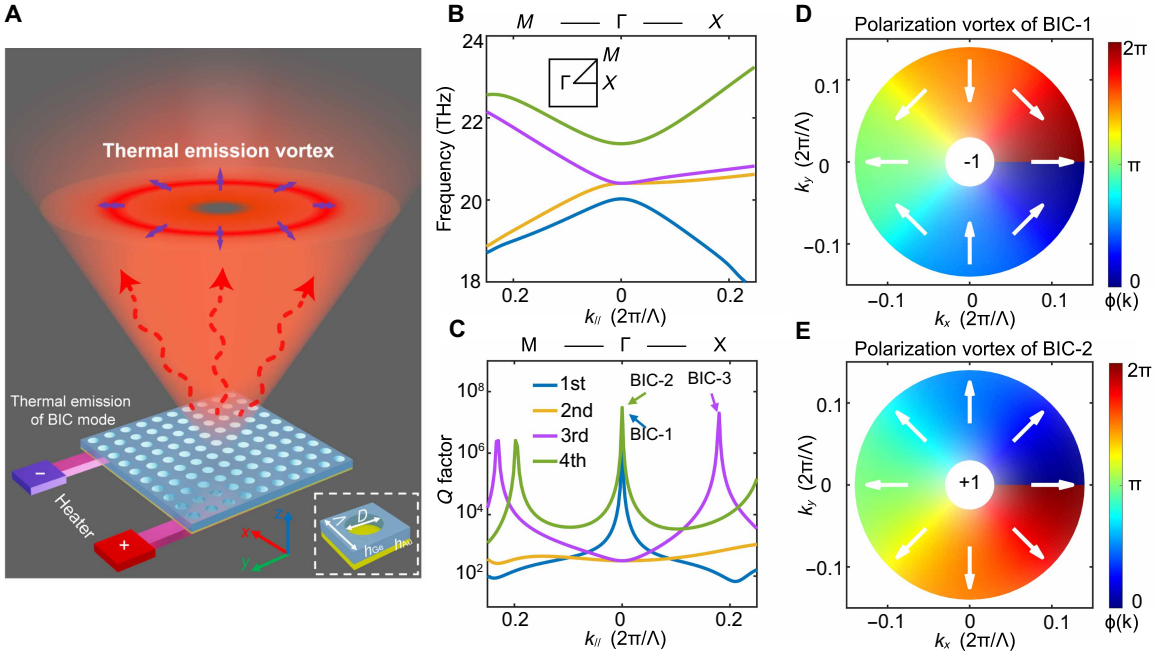

Fig. 1. PVTE realized with BICs in a PCS. (**A**) Schematic of the designed PCS illustrating the generation of different linearly polarized thermal emissions in distinct directions. (**B**) Simulated band structure of the PCS along the Γ-*X* and Γ-*M* directions. The inset depicts the first Brillouin zone. (**C**) Calculated *Q* factor of the four bands, with the BICs of interest indicated by arrows. (**D** and **E**) Polarization vortices of BIC-1 and BIC-2 in momentum space, characterized by topological charges −1 and +1, respectively. The color representation signifies the angle of linear polarization relative to the horizontal line, and specific polarization vectors are denoted by white arrows.

to the thickness of the Ge slab), is etched on the Ge slab. In this PCS, the uniform Au layer can effectively block thermal emission from the substrate, ensuring the thermal emission predominantly arises from the guided resonance modes of the PCS. Simulated band dispersions along high symmetric directions are shown in Fig. 1B, which belong to the infrared regime (from 18 to 26 THz). In this range, Ge is approximated as a lossless dielectric material with a refractive index of $n = 4.06$, while Au is modeled with the lossless Drude model (neglecting ohmic loss for simplification). Notably, the four bands in Fig. 1B are all above the light cone, allowing for radiation to free space.

The system under consideration exhibits $\mathbf{C_{4v}}$ point group symmetry, where the states of two nondegenerate bands—specifically the first and fourth bands at the Γ point—represent BICs with divergent *Q* factors in Fig. 1C. These BICs, identified as BIC-1 and BIC-2, are commonly referred to symmetry-protected BICs (*43*). In addition, there are accidental BICs (*44*) along the high symmetric directions, as indicated by the peaks in the *Q* factors. The electric field distributions of the targeted BICs exhibit the corresponding symmetry representations of the $\mathbf{C_{4v}}$ group (see fig. S1). Later on, we will investigate the BIC on the third band along the Γ-*X* direction, marked by the purple arrow and labeled as BIC-3.

The characterization of polarization vortices associated with BICs hinges upon their distinctive topological charges. The topological charge of a BIC is formally defined as

$$q = \frac{1}{2\pi}\oint_C dk \cdot \nabla_k \phi(k) \quad q \in \mathbb{Z} \tag{1}$$

Here, $\phi(k)$ represents the angle of the polarization vector that radiated into the surrounding air (the direction of the long axis in the case of elliptical polarization), and *C* is a closed loop that encircles the BIC in the counterclockwise direction. Because of the up-down symmetry and $\mathbf{C_2}$ symmetry of PCS, the modes are linearly polarized near the Γ point (*62*). We set the far-field domain in COMSOL to calculate $\phi(k)$, and the simulated results are visualized with color maps in Fig. 1 (D and E). White arrows are used to emphasize specific polarization vectors. In accordance with Eq. 1, the topological charges of BIC-1 and BIC-2 are conclusively determined as −1 and +1, corresponding to a total accumulated winding angle of -2π and $+2\pi$, respectively. From the perspective of group theory, the allowed charges under $\mathbf{C_{4v}}$ symmetry correspond to different irreducible representations (*63*), thereby manifesting distinct polarization vortices (see fig. S2). Because of topological protection, the polarization vortices exhibit strong robustness to variations in structural parameters (see fig. S3).

Experimental setup and measurement

To calibrate the emission field concerning both angle and polarization, we used an enhanced in-house PARTES in Fig. 2A, enabling both polarization and angular resolution for thermal emission compared to the system in our previous work (*64*). The heating stage (Linkam FTIR 600) holds the temperature of the sample (see the scanning electron microscopy image in Fig. 2B) at 100°C. The inset highlights a two-axis rotation stage in combination with the heating stage, enabling precise control over the emission direction. Rotation angles, θ and φ, are defined with respect to the *y* axis and *z* axis, respectively. The emitted field traverses a mid-infrared linear polarizer (Thorlabs, WP25H-Z) before reaching a Fourier transform infrared (FTIR) spectrometer (Bruker Vertex 70). The linear polarizer dictates the polarization direction, and the FTIR facilitates the

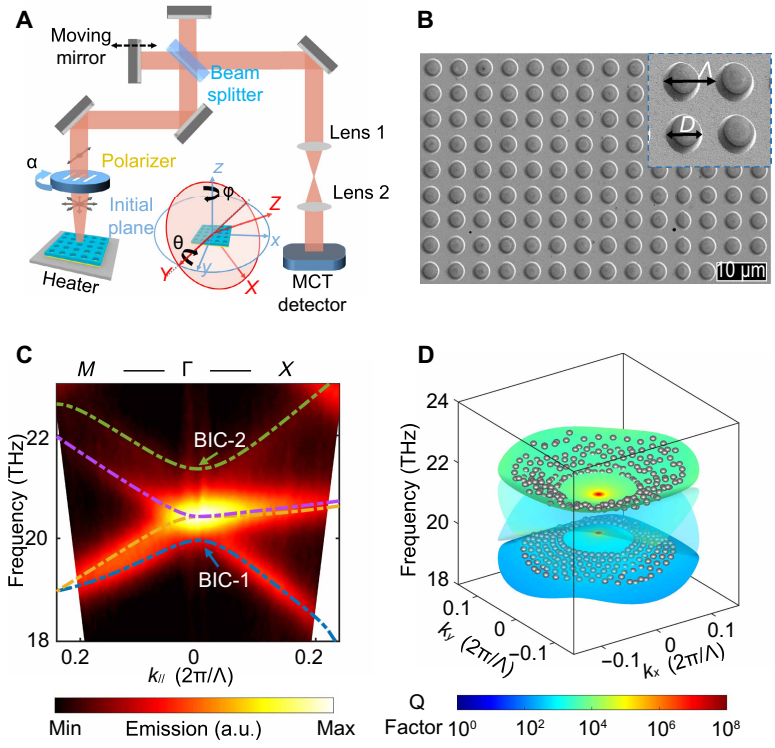

Fig. 2. Unpolarized measurement of the PVTE. (**A**) Experimental setup of PARTES, featuring a heating stage integrated with a two-dimensional rotating stage, a mid-infrared linear polarizer, and an FTIR. (**B**) Scanning electron microscopy image depicting the fabricated PCS. (**C**) Measured band structure along *M*-Γ-*X* direction, with two BICs indicated by arrows. (**D**) Dispersion of the first and fourth bands in the momentum space, with gray spheres denoting extracted data from measured thermal emission. Colored surfaces represent simulated dispersion, with color indicating the *Q* factor. a.u., arbitrary units.

calibration of thermal emission spectra in the mid-infrared range, featuring a spectral resolution of 1 cm^{-1}.

We initially excluded the polarizer (temporarily) and conducted measurements of angle-resolved emission spectra encompassing all polarization states along the *M*-Γ-*X* direction. As shown in Fig. 2C, the thermal emission intensity (after subtracting the emission of a Ge slab), highlighted by vibrant colors, occurs prominently around the resonance modes of the PCS, as indicated by the dashed lines. Notably, the emission intensity from the fourth band is relatively subdued compared to that from other bands, being more evident upon closer examination. The color map displays darkness for frequencies away from the resonance modes, indicating a clear background. Arrows pinpoint the positions of two BICs located on the first and fourth bands, where the signals appear comparatively weaker than those of neighboring states. All the above experimental results align well with the simulations (see fig. S4).

When isolating the resonance modes, the peaks of the emission spectra allow us to extract the mode dispersions in *k*-space. Through further tuning (θ and φ), we conducted measurements of thermal emission in the two-dimension momentum space (see fig. S5) and extracted the peaks near the first and fourth bands. The measured dispersions are illustrated in Fig. 2D, with each gray sphere indicating the central frequency of a peak, and the simulated dispersions are presented with colored surfaces for comparison, where the color represents the *Q* factor of the resonance mode. As the thermal emission weakens when approaching the BICs, particularly the Γ point, identifying peaks becomes challenging; hence, the experimental data near this region are omitted. Nevertheless, the gray spheres almost perfectly match well with the surfaces, indicating a high degree of agreement. The measured *Q* factor also increase as approaching the BICs (see fig. S6). Note here that, to realize an effective thermal emitter, we are not aiming at the states with highest *Q* factor. Instead, the maximum thermal flux is achieved when the radiative loss matches the intrinsic material loss (*65*).

Polarization vortices of symmetry-protected BICs

To further characterize the polarization states around the BICs, a mid-infrared linear polarizer positioned at an angle α to the horizontal line was reintroduced between the thermal emitter and the FTIR during the measurement of angle-resolved spectra. The polarization-dependent thermal emission spectra are presented for α = 0° (left) and 90° (right), with φ = 0° and 45° in Fig. 3 (A and B). Simulated dispersions are included with dashed lines for reference. These thermal emission spectra allow for the determination of polarization states. For example, in Fig. 3A, the intensities of the first and fourth bands at α = 0° are considerably higher than those at α = 90°, indicating that the polarization vectors of the first and fourth bands align approximately along the *x* direction. However, because of the absence of phase information in the spectra, there remains uncertainty in determining the exact polarization direction—whether it lies in the first or fourth quarter. To resolve this ambiguity, we conducted measurements for two sets of orthogonal polarization

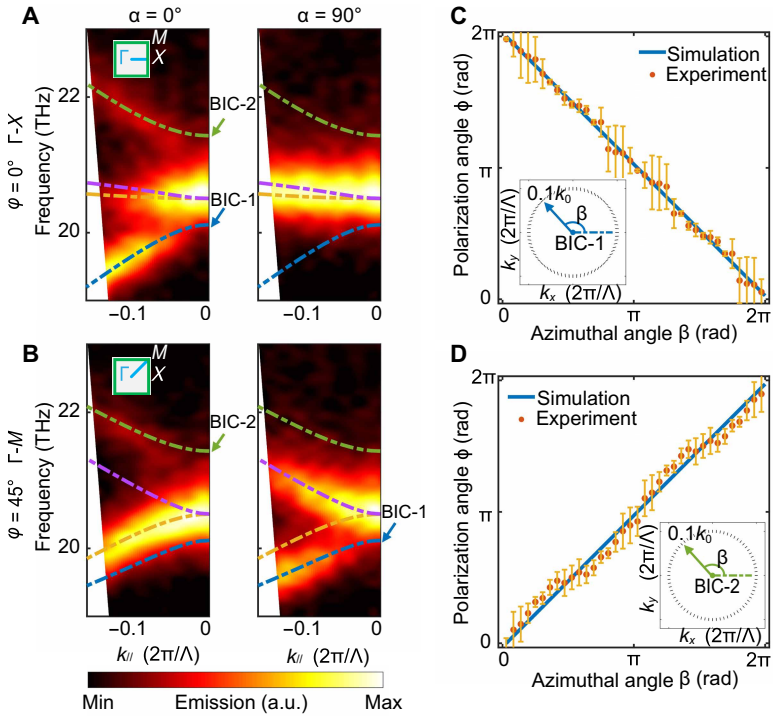

Fig. 3. Measured polarization vortices of symmetry-protected BICs. (**A** and **B**) Measured thermal emission spectra with two different polarizations (α = 0° and α = 90°) along φ = 0° and φ = 45° directions. The insets indicate the directions that φ angles correspond to. (**C** and **D**) Measured polarization angles versus azimuthal angles that encircle the BICs. Dots with error bars represent experimental data, and solid lines depict simulated results. Insets illustrate the loop used for identifying the polarization vortices.

directions. In experiments, α values were set to 0° and 90° and 45° and 135° (see fig. S7), and the orthogonal pairs were used to identify the linear polarization of the state and the error bar (see fig. S8).

We chose a loop (satisfying $k_x^2 + k_y^2 = 0.1^2$) that encloses the BIC in the counterclockwise direction, defined as azimuthal angle β, and plotted the corresponding polarization angle ϕ in Fig. 3 (C and D). As the PCS here exhibits $\mathbf{C_4}$ symmetry, we have measured the thermal emission from 0° to 90°, and others were determined according to $\mathbf{C_4}$ symmetry. The dots with error bars represent measured polarization angles, while the blue lines depict simulated results that continuously evolve within the range of 0-2π. The simulated results exhibit almost straight lines, indicating that polarization angles near the Γ point can be approximated by $\phi(k) = \arg(k_x \mp ik_y)$ for the first and fourth bands. Here, the "∓" represents the charge (winding) of the polarization vortex, with values of −1 and +1 for the first and fourth bands, respectively. The experimental data match well with the theoretical angles, confirming the experimental observation of the PVTE. For other BICs with different representations of $\mathbf{C_{4v}}$, such as $\mathbf{A_2}$ and $\mathbf{B_2}$, the polarization vortices with different polarization distribution (*52*, *66*) of the thermal emission can be similarly mapped out.

Polarization vortex of an accidental BIC

Besides the symmetry-protected BICs located at the Γ point, this PCS also features a single-resonance BIC (designated as BIC-3 in Fig. 1B) at $k_x = 0.17$ in the third band. This accidental BIC has a topological charge of +1 and remains robust due to the $\mathbf{C_2}$ symmetry, exhibiting slight shifts under variations in the structural parameters (see fig. S9). As BIC-3 carries a nonzero charge, a corresponding polarization vortex is expected to surround it. The second and third bands are doubly degenerate at the Γ point, belonging to the **E** representation of the $\mathbf{C_{4v}}$ point group. This degeneracy is lifted and splits into one **A**-mode (*x*-polarized) and one **B**-mode (*y*-polarized) along the Γ-*X* direction, resulting in a minor bandgap as shown in Fig. 4A. Although this small bandgap remains imperceptible in unpolarized spectra due to the finite bandwidth of thermal emission, polarization-dependent spectra provides a means to differentiate the two bands by tuning the parameter α.

As required by the corresponding symmetry representation, the emission spectra are E_x-dominated and E_y-dominated for the second and third bands, corresponding to α = 0° and α = 90° as displayed in Fig. 4B, respectively. It is evident that there is one dark mode at $k_x = 0.17$ in the left, as marked by the purple arrow, while no dark mode is observed in the right. This dark mode indicates the position of the accidental BIC. We extracted the peak intensities of the measured emission at α = 0° and 90°, shown with black and red open circles in Fig. 4C. Because of unavoidable environmental noise (e.g., thermal emission from the surrounding air), the intensity does not reach exactly zero at BIC-3. The behaviors of measured data are quite similar to the simulated intensities (red and black lines), with the lowest value occurring at $k_x = 0.17$.

After determining the polarization states along the Γ-*X* line, we measured the polarization vectors of the thermal emission around the BIC-3, as plotted in Fig. 4D, tracing the loop of wave vectors depicted in the inset. The dots with error bars represent the measured

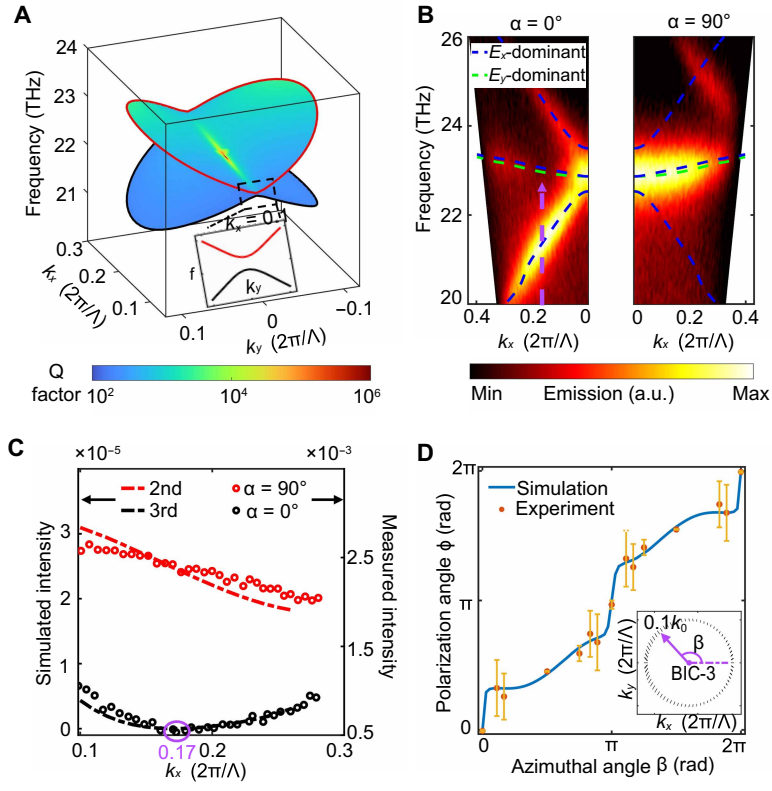

Fig. 4. Polarization vortex of an accidental BIC. (**A**) Dispersion of the second and third bands near BIC-3 under consideration. Color indicates the *Q* factor. (**B**) Measured thermal emission spectra with orthogonal polarizations (α = 0° and α = 90°). Dashed lines represent the simulated dispersions. (**C**) Measured intensities (open circles) for the second and third bands with two α. Dashed lines indicate simulated results. (**D**) Measured polarization angles versus azimuthal angles encircling the BICs. Dots with error bars represent experimental data, and solid lines depict simulated results. The inset illustrates the loop for measuring the polarization vortex.

data, while the solid blue lines denote the simulated results. In simulations, polarization states are in general elliptically polarized with very small ellipticity (almost linearly polarized) (*62*), and the direction of the long axis of the elliptical polarization changes rapidly versus the azimuthal angles β around 0° and 180°. Because of the mini-gap between the second and third bands, distinguishing elliptical states becomes challenging in experiments. States away from the symmetry line, as measured in experiments, tend to display linear polarizations, with a gradual shift in the polarization angles. The close match between the dots and the line confirms that the topological charge of BIC-3 is +1, accompanied by a polarization vortex similar to those of Γ-BICs but at controllable different radiation directions.

DISCUSSION

Our device offers notable enhancements in flexibility, scalability, and ease of fabrication while providing distinct advantages in robust and continuous polarization control of thermal emission compared to existing works. Furthermore, in scenarios involving broken C_2 symmetry, the PVTE has the potential to produce all-polarized emissions, spanning the entire Poincaré sphere (*53*). Our work paves the way for extensive exploration in the realm of thermal emission combined with BICs. Future investigations could delve into high-order BICs, the evolutionary patterns of BICs, and the emergence of multiple BICs, providing valuable insights for manipulating thermal emission.

In summary, we realize a PVTE based on BICs in a PCS. By encircling BICs in momentum space, arbitrary linear polarizations can be generated from a single PVTE. Using a self-developed PARTES, we experimentally measure the polarization vortices of thermal emission originating from BICs. This PVTE can accommodate multiple polarization vortices for various types and charges of BICs, enabling broadband frequency and polarization selection in the infrared region. Without the need for external infrared laser sources, our PVTE holds promise for direct integration into on-chip applications, such as microthermal imaging, microinfrared sensing, on-chip information encryption, and related domains. Our work presents additional pathways for controlling thermal emission and may offer valuable insights for designing advanced thermal emitters.

MATERIALS AND METHODS

Fabrication of PCSs

The PCSs investigated in this work were fabricated using ultraviolet lithography and electron beam evaporation techniques. A 200-nm-thick gold (Au) layer was deposited on a silicon substrate through electron beam evaporation. The designed patterns were subsequently transferred from a chromium (Cr) mask to a spin-coated photoresist film (RPN-1150) with a thickness sufficient for the subsequent steps using ultraviolet lithography. Germanium (Ge) was then deposited via vacuum evaporation, and any remaining photoresist was

removed with *N*-methyl-pyrrolidone. To achieve sufficiently pronounced thermal emission, the samples had size of 2 cm by 2 cm, totaling 16 million unit cells.

Details about the home-made PARTES

The PARTES setup comprised a heating stage (Linkam, FTIR 600) integrated with a self-developed rotation stage, a mid-infrared linear polarizer (Thorlabs, WP25H-Z), and an FTIR spectrometer (Bruker, Vertex 70). This system facilitated precise calibration of angle and polarization resolutions in the study of thermal emission. The heating stage maintained the sample temperature at a constant 100°C with a high precision of 0.1°C. The rotation stage, consisting of a motorized rotator (an accuracy of 0.1°) and a manual rotator (an accuracy of 1°), provided a wide rotation range in two planes. Positioned in front of the FTIR, the mid-infrared linear polarizer, with its polarization orientation represented by the angle α relative to the horizontal line, was adjusted to discern the polarization state of thermal emission. Emission spectra were captured using the FTIR spectrometer, offering a spectral resolution of 1 cm^{-1}. To minimize system noise, a liquid nitrogen–cooled mercury cadmium telluride (MCT) detector was used, and simultaneous nitrogen purging was conducted in a closed experimental system. Furthermore, the PARTES measurement system can also measure the circularly polarized thermal emission when integrated with a wave plate.

Polarization analysis

In this work, we use BICs in the momentum space to generate polarization vortices of thermal emission. Therefore, it is essential to convert the measured physical quantities between real space and momentum space.

As shown in fig. S5, the emission angle φ corresponds to the direction of the in-plane wave vector $k_{\parallel}$ in momentum space. At a fixed emission angle φ, the orientation of the polarizer α (0°/45°/90°/135°) is defined relative to the direction of wave vector $k_{\parallel}$, as illustrated in fig. S8. Accordingly, to reconstruct the polarization states in momentum space, both φ and α must be considered together. Moreover, since the measured thermal emission intensity is a scalar quantity, it cannot fully capture the vector nature of polarization when projected into momentum space. To ensure the reliability of polarization reconstruction, we consider the result valid only when consistent polarization states are obtained using two orthogonal polarizer bases, i.e., $\alpha = 0°$ and 90° and $\alpha = 45°$ and 135°.

Given that the intensity of thermal emission is a scalar value, we inferred the direction of the electric field by using the measured intensity of thermal emission (I), emission angle (φ), and the polarization orientation (α), expressed as

$$\vec{E}_i = \pm\sqrt{I_i}\cdot\left[\cos\left(\varphi+\alpha_i\right)\cdot\vec{e}_x+\sin\left(\varphi+\alpha_i\right)\cdot\vec{e}_y\right] \quad (2)$$

Here, i indicates the index of angle $\alpha = [0°, 45°, 90°, 135°]$, and $\vec{e}_x$ and $\vec{e}_y$ are the basic vectors in the k_x-k_y plane. Thus, for the orthogonal sets of α, the possible synthesized polarization vectors can be described as

$$\left[\vec{E}_1+\vec{E}_3;\vec{E}_1-\vec{E}_3;\vec{E}_2+\vec{E}_4;\vec{E}_2-\vec{E}_4\right] \quad (3)$$

For a specific polarization, one identical vector can be obtained by the two orthogonal sets. Comparing the four composite vectors, we chose the two with the smallest difference, considering them to be the closest to the actual values—such as $\vec{S}_{1B}$ in fig. S8A and $\vec{S}_{2A}$ in fig. S8B. The representation of the polarization state of thermal emission was determined by the average vector of $\vec{S}_{1B}$ and $\vec{S}_{2A}$, and the difference between them was defined as the error bar in experiments.

The overlap between different resonant modes has a more pronounced effect on the extraction of the polarization angle as it influences the accuracy of the emission intensity extraction. The details of how we extract the polarization direction is presented in section S7 (see eqs. S2 to S4). Such a scheme is based on the measurement of the peak emission intensity on four polarization angles (α). As the spectra of thermal emission broadens, extracting emission intensity for one band becomes influenced by other nearby bands, leading to considerably larger error than the other factors in our measurement.

Supplementary Materials

This PDF file includes:

Figs. S1 to S9
Supplementary Text
Tables S1 and S2
References

REFERENCES AND NOTES

1. T. Liu, C. Guo, W. Li, S. Fan, Thermal photonics with broken symmetries. *eLight* **2**, 25 (2022).
2. Q. Q. Chu, F. Zhong, X. H. Shang, Y. Zhang, S. N. Zhu, H. Liu, Controlling thermal emission with metasurfaces and its applications. *Nanophotonics* **13**, 1279–1301 (2024).
3. S. Yang, M. Liu, C. Zhao, S. Fan, C.-W. Qiu, Nonreciprocal thermal photonics. *Nat. Photonics* **18**, 412–424 (2024).
4. J.-J. Greffet, R. Carminati, K. Joulain, J.-P. Mulet, S. Mainguy, Y. Chen, Coherent emission of light by thermal sources. *Nature* **416**, 61–64 (2002).
5. O. Ilic, P. Bermel, G. Chen, J. D. Joannopoulos, I. Celanovic, M. Soljačić, Tailoring high-temperature radiation and the resurrection of the incandescent source. *Nat. Nanotechnol.* **11**, 320–324 (2016).
6. A. P. Raman, M. A. Anoma, L. Zhu, E. Rephaeli, S. Fan, Passive radiative cooling below ambient air temperature under direct sunlight. *Nature* **515**, 540–544 (2014).
7. Y. Zhai, Y. Ma, S. N. David, D. Zhao, R. Lou, G. Tan, R. Yang, X. Yin, Scalable-manufactured randomized glass-polymer hybrid metamaterial for daytime radiative cooling. *Science* **355**, 1062–1066 (2017).
8. D. Li, X. Liu, W. Li, Z. Lin, B. Zhu, Z. Li, J. Li, B. Li, S. Fan, J. Xie, J. Zhu, Scalable and hierarchically designed polymer film as a selective thermal emitter for high-performance all-day radiative cooling. *Nat. Nanotechnol.* **16**, 153–158 (2021).
9. S. Zeng, S. Pian, M. Su, Z. Wang, M. Wu, X. Liu, M. Chen, Y. Xiang, J. Wu, M. Zhang, Q. Cen, Y. Tang, X. Zhou, Z. Huang, R. Wang, A. Tunuhe, X. Sun, Z. Xia, M. Tian, M. Chen, X. Ma, L. Yang, J. Zhou, H. Zhou, Q. Yang, X. Li, Y. Ma, G. Tao, Hierarchical-morphology metafabric for scalable passive daytime radiative cooling. *Science* **373**, 692–696 (2021).
10. A. Lenert, D. M. Bierman, Y. Nam, W. R. Chan, I. Celanović, M. Soljačić, E. N. Wang, A nanophotonic solar thermophotovoltaic device. *Nat. Nanotechnol.* **9**, 126–130 (2014).
11. A. Lochbaum, Y. Fedoryshyn, A. Dorodnyy, U. Koch, C. Hafner, J. Leuthold, On-chip narrowband thermal emitter for mid-IR optical gas sensing. *ACS Photonics* **4**, 1371–1380 (2017).
12. Y. Qu, Q. Li, L. Cai, M. Pan, P. Ghosh, K. Du, M. Qiu, Thermal camouflage based on the phase-changing material GST. *Light Sci. Appl.* **7**, 26 (2018).
13. O. Salihoglu, H. B. Uzlu, O. Yakar, S. Aas, O. Balci, N. Kakenov, S. Balci, S. Olcum, S. Süzer, C. Kocabas, Graphene-based adaptive thermal camouflage. *Nano Lett.* **18**, 4541–4548 (2018).
14. M. De Zoysa, T. Asano, K. Mochizuki, A. Oskooi, T. Inoue, S. Noda, Conversion of broadband to narrowband thermal emission through energy recycling. *Nat. Photonics* **6**, 535–539 (2012).
15. X. Liu, T. Tyler, T. Starr, A. F. Starr, N. M. Jokerst, W. J. Padilla, Taming the blackbody with infrared metamaterials as selective thermal emitters. *Phys. Rev. Lett.* **107**, 045901 (2011).
16. X. Zhang, H. Liu, Z. G. Zhang, Q. Wang, S. N. Zhu, Controlling thermal emission of phonon by magnetic metasurfaces. *Sci. Rep.* **7**, 41858 (2017).
17. X. Zhang, Z. Zhang, Q. Wang, S. Zhu, H. Liu, Controlling thermal emission by parity-symmetric fano resonance of optical absorbers in metasurfaces. *ACS Photonics* **6**, 2671–2676 (2019).

18. J. Xu, J. Mandal, A. P. Raman, Broadband directional control of thermal emission. *Science* **372**, 393–397 (2021).
19. R. St-Gelais, L. Zhu, S. Fan, M. Lipson, Near-field radiative heat transfer between parallel structures in the deep subwavelength regime. *Nat. Nanotechnol.* **11**, 515–519 (2016).
20. J. Yang, W. Du, Y. Su, Y. Fu, S. Gong, S. He, Y. Ma, Observing of the super-Planckian near-field thermal radiation between graphene sheets. *Nat. Commun.* **9**, 4033 (2018).
21. Y. Hadad, J. C. Soric, A. Alu, Breaking temporal symmetries for emission and absorption. *Proc. Natl. Acad. Sci. U.S.A.* **113**, 3471–3475 (2016).
22. K. J. Shayegan, S. Biswas, B. Zhao, S. Fan, H. A. Atwater, Direct observation of the violation of Kirchhoff's law of thermal radiation. *Nat. Photonics* **17**, 891–896 (2023).
23. M. Liu, S. Xia, W. Wan, J. Qin, H. Li, C. Zhao, L. Bi, C. W. Qiu, Broadband mid-infrared non-reciprocal absorption using magnetized gradient epsilon-near-zero thin films. *Nat. Mater.* **22**, 1196–1202 (2023).
24. J. A. Schuller, T. Taubner, M. L. Brongersma, Optical antenna thermal emitters. *Nat. Photonics* **3**, 658–661 (2009).
25. N. Shitrit, I. Yulevich, E. Maguid, D. Ozeri, D. Veksler, V. Kleiner, E. Hasman, Spin-optical metamaterial route to spin-controlled photonics. *Science* **340**, 724–726 (2013).
26. S. A. Dyakov, V. A. Semenenko, N. A. Gippius, S. G. Tikhodeev, Magnetic field free circularly polarized thermal emission from a chiral metasurface. *Phys. Rev. B* **98**, 235416 (2018).
27. L. Wojszvzyk, A. Nguyen, A.-L. Coutrot, C. Zhang, B. Vest, J.-J. Greffet, An incandescent metasurface for quasimonochromatic polarized mid-wave infrared emission modulated beyond 10 MHz. *Nat. Commun.* **12**, 1492 (2021).
28. Q. Q. Chu, F. Y. Zhang, Y. Zhang, T. Qiao, S. N. Zhu, H. Liu, Integrated thermal emission microchip based on meta-cavity array. *Nanophotonics* **11**, 4263–4271 (2022).
29. A. Nguyen, J.-P. Hugonin, A.-L. Coutrot, E. Garcia-Caurel, B. Vest, J.-J. Greffet, Large circular dichroism in the emission from an incandescent metasurface. *Optica* **10**, 232–238 (2023).
30. X. Wang, T. Sentz, S. Bharadwaj, S. K. Ray, Y. Wang, D. Jiao, L. Qi, Z. Jacob, Observation of nonvanishing optical helicity in thermal radiation from symmetry-broken metasurfaces. *Sci. Adv.* **9**, eade4203 (2023).
31. L. P. Wang, Z. M. Zhang, Wavelength-selective and diffuse emitter enhanced by magnetic polaritons for thermophotovoltaics. *Appl. Phys. Lett.* **100**, 063902 (2012).
32. B. Zhao, J. M. Zhao, Z. M. Zhang, Enhancement of near-infrared absorption in graphene with metal gratings. *Appl. Phys. Lett.* **105**, 031905 (2014).
33. J. Kim, K. Han, J. W. Hahn, Selective dual-band metamaterial perfect absorber for infrared stealth technology. *Sci. Rep.* **7**, 6740 (2017).
34. J. R. Nolen, A. C. Overvig, M. Cotrufo, A. Alù, Local control of polarization and geometric phase in thermal metasurfaces. *Nat. Nanotechnol.* **19**, 1627–1634 (2024).
35. M. R. Dennis, K. O'Holleran, M. J. Padgett, Singular optics: Optical vortices and polarization singularities. *Prog. Opt.* **53**, 293–363 (2009).
36. Y. Shen, X. Wang, Z. Xie, C. Min, X. Fu, Q. Liu, M. Gong, X. Yuan, Optical vortices 30 years on: OAM manipulation from topological charge to multiple singularities. *Light Sci. Appl.* **8**, 90 (2019).
37. C. W. Hsu, B. Zhen, A. D. Stone, J. D. Joannopoulos, M. Soljačić, Bound states in the continuum. *Nat. Rev. Mater.* **1**, 16048 (2016).
38. X. Gao, C. W. Hsu, B. Zhen, X. Lin, J. D. Joannopoulos, M. Soljačić, H. Chen, Formation mechanism of guided resonances and bound states in the continuum in photonic crystal slabs. *Sci. Rep.* **6**, 31908 (2016).
39. K. Koshelev, S. Lepeshov, M. Liu, A. Bogdanov, Y. Kivshar, Asymmetric metasurfaces with high-Q resonances governed by bound states in the continuum. *Phys. Rev. Lett.* **121**, 193903 (2018).
40. J. Jin, X. Yin, L. Ni, M. Soljačić, B. Zhen, C. Peng, Topologically enabled ultrahigh-Q guided resonances robust to out-of-plane scattering. *Nature* **574**, 501–504 (2019).
41. M. Kang, S. Zhang, M. Xiao, H. Xu, Merging bound states in the continuum at off-high symmetry points. *Phys. Rev. Lett.* **126**, 117402 (2021).
42. D. C. Marinica, A. G. Borisov, S. V. Shabanov, Bound states in the continuum in photonics. *Phys. Rev. Lett.* **100**, 183902 (2008).
43. Y. Plotnik, O. Peleg, F. Dreisow, M. Heinrich, S. Nolte, A. Szameit, M. Segev, Experimental observation of optical bound states in the continuum. *Phys. Rev. Lett.* **107**, 183901 (2011).
44. C. W. Hsu, B. Zhen, J. Lee, S.-L. Chua, S. G. Johnson, J. D. Joannopoulos, M. Soljačić, Observation of trapped light within the radiation continuum. *Nature* **499**, 188–191 (2013).
45. Y.-X. Xiao, G. Ma, Z.-Q. Zhang, C. T. Chan, Topological subspace-induced bound state in the continuum. *Phys. Rev. Lett.* **118**, 166803 (2017).
46. M. Kang, T. Liu, C. T. Chan, M. Xiao, Applications of bound states in the continuum in photonics. *Nat. Rev. Phys.* **5**, 659–678 (2023).
47. A. Kodigala, T. Lepetit, Q. Gu, B. Bahari, Y. Fainman, B. Kanté, Lasing action from photonic bound states in continuum. *Nature* **541**, 196–199 (2017).
48. M.-S. Hwang, H.-C. Lee, K.-H. Kim, K.-Y. Jeong, S.-H. Kwon, K. Koshelev, Y. Kivshar, H.-G. Park, Ultralow-threshold laser using super-bound states in the continuum. *Nat. Commun.* **12**, 4135 (2021).
49. Z. Liu, Y. Xu, Y. Lin, J. Xiang, T. Feng, Q. Cao, J. Li, S. Lan, J. Liu, High-Q quasibound states in the continuum for nonlinear metasurfaces. *Phys. Rev. Lett.* **123**, 253901 (2019).
50. V. Ardizzone, F. Riminucci, S. Zanotti, A. Gianfrate, M. Efthymiou-Tsironi, D. G. Suàrez-Forero, F. Todisco, M. De Giorgi, D. Trypogeorgos, G. Gigli, K. Baldwin, L. Pfeiffer, D. Ballarini, H. S. Nguyen, D. Gerace, D. Sanvitto, Polariton Bose–Einstein condensate from a bound state in the continuum. *Nature* **605**, 447–452 (2022).
51. B. Zhen, C. W. Hsu, L. Lu, A. D. Stone, M. Soljačić, Topological nature of optical bound states in the continuum. *Phys. Rev. Lett.* **113**, 257401 (2014).
52. Y. Zhang, A. Chen, W. Liu, C. W. Hsu, B. Wang, F. Guan, X. Liu, L. Shi, L. Lu, J. Zi, Observation of polarization vortices in momentum space. *Phys. Rev. Lett.* **120**, 186103 (2018).
53. W. Liu, B. Wang, Y. Zhang, J. Wang, M. Zhao, F. Guan, X. Liu, L. Shi, J. Zi, Circularly polarized states spawning from bound states in the continuum. *Phys. Rev. Lett.* **123**, 116104 (2019).
54. X. Yin, J. Jin, M. Soljačić, C. Peng, B. Zhen, Observation of topologically enabled unidirectional guided resonances. *Nature* **580**, 467–471 (2020).
55. A. Overvig, N. Yu, A. Alù, Chiral quasi-bound states in the continuum. *Phys. Rev. Lett.* **126**, 073001 (2021).
56. T. Shi, Z. L. Deng, G. Geng, X. Zeng, Y. Zeng, G. Hu, A. Overvig, J. Li, C. W. Qiu, A. Alu, Y. S. Kivshar, X. Li, Planar chiral metasurfaces with maximal and tunable chiroptical response driven by bound states in the continuum. *Nat. Commun.* **13**, 4111 (2022).
57. X. Zhang, Y. Liu, J. Han, Y. Kivshar, Q. Song, Chiral emission from resonant metasurfaces. *Science* **377**, 1215–1218 (2022).
58. Y. Chen, H. Deng, X. Sha, W. Chen, R. Wang, Y. H. Chen, D. Wu, J. Chu, Y. S. Kivshar, S. Xiao, C. W. Qiu, Observation of intrinsic chiral bound states in the continuum. *Nature* **613**, 474–478 (2023).
59. C. Huang, C. Zhang, S. Xiao, Y. Wang, Y. Fan, Y. Liu, N. Zhang, G. Qu, H. Ji, J. Han, L. Ge, Y. Kivshar, Q. Song, Ultrafast control of vortex microlasers. *Science* **367**, 1018–1021 (2020).
60. S. Han, J. Cui, Y. Chua, Y. Zeng, L. Hu, M. Dai, F. Wang, F. Sun, S. Zhu, L. Li, A. G. Davies, E. H. Linfield, C. S. Tan, Y. Kivshar, Q. J. Wang, Electrically-pumped compact topological bulk lasers driven by band-inverted bound states in the continuum. *Light Sci. Appl.* **12**, 145 (2023).
61. B. Wang, W. Liu, M. Zhao, J. Wang, Y. Zhang, A. Chen, F. Guan, X. Liu, L. Shi, J. Zi, Generating optical vortex beams by momentum-space polarization vortices centred at bound states in the continuum. *Nat. Photonics* **14**, 623–628 (2020).
62. C. W. Hsu, B. Zhen, M. Soljačić, A. D. Stone, Polarization state of radiation from a photonic crystal slab. arXiv:1708.02197 [physics.optics] (2017).
63. J. Wang, X. Wang, Z. Wu, X. Zhao, S. Wu, L. Shi, Y. Kivshar, J. Zi, Inherent spin-orbit locking in topological lasing via bound state in the continuum. *Phys. Rev. Lett.* **134**, 133802 (2025).
64. F. Zhong, K. Ding, Y. Zhang, S. Zhu, C. T. Chan, H. Liu, Angle-resolved thermal emission spectroscopy characterization of non-Hermitian metacrystals. *Phys. Rev. Appl.* **13**, 014071 (2020).
65. L. Zhu, S. Sandhu, C. Otey, S. Fan, M. B. Sinclair, T. Shan Luk, Temporal coupled mode theory for thermal emission from a single thermal emitter supporting either a single mode or an orthogonal set of modes. *Appl. Phys. Lett.* **102**, 103104 (2013).
66. M. Kang, L. Mao, S. Zhang, M. Xiao, H. Xu, C. T. Chan, Merging bound states in the continuum by harnessing higher-order topological charges. *Light Sci. Appl.* **11**, 228 (2022).
67. Z.-Y. Yang, S. Ishii, T. Yokoyama, T. D. Dao, M.-G. Sun, P. S. Pankin, I. V. Timofeev, T. Nagao, K.-P. Chen, Narrowband wavelength selective thermal emitters by confined Tamm plasmon polaritons. *ACS Photonics* **4**, 2212–2219 (2017).
68. S. Yang, M. He, C. Hong, J. Nordlander, J.-P. Maria, J. D. Caldwell, J. C. Ndukaife, Single-peak and narrow-band mid-infrared thermal emitters driven by mirror-coupled plasmonic quasi-BIC metasurfaces. *Optica* **11**, 305–314 (2024).
69. K. Sakoda, *Optical Properties of Photonic Crystals* (Springer, ed. 2, 2005), vol. 2.
70. Z. Zhai, Z. Li, Y. Du, X. Gan, L. He, X. Zhang, Y. Zhou, J. Guan, Y. Cai, X. Ao, Multimode vortex lasing from Dye–TiO_2 lattices via bound states in the continuum. *ACS Photonics* **10**, 437–446 (2023).

Acknowledgments: We thank K. Gao, X. Shang, and Y. Xiao for valuable discussions.
Funding: This work was financially supported by the National Key R&D Program of China (nos. 2024YFA1210500 and 2023YFA1407600), the National Natural Science Foundation of China (nos. 92150302, 92163216, 12334015, 62288101, 12321161645, and 12004072), and the Natural Science Foundation of Jiangsu Province (nos. BK20243009 and BK20233001). **Author contributions:** Conceptualization: H.L. Numerical simulations: Y.Z. and Q.W. Fabrication and measurement: Y.Z. and Z.L. Data analysis: Y.Z., Q.W., M.X., T.L., F.Z., and H.L. Writing: Y.Z., Q.W., M.X., and H.L. Supervision: H.L. and S.Z. **Competing interests:** The authors declare that they have no competing interests. **Data and materials availability:** All data needed to evaluate the conclusions in the paper are present in the paper and/or the Supplementary Materials.

Submitted 24 March 2025
Accepted 19 August 2025
Published 19 September 2025
10.1126/sciadv.adx6252